ACSNANO

www.acsnano.org

Article

A "Jack-of-All-Trades" Phototheranostic System Enabled by Strategic Regulation of Ferroptosis and PANoptosis for Cancer Therapy

Xiaoli Lu,[▽] Lan Xie,[▽] Huan Yu,[▽] Yunfei Zuo, Guokang He, Jinyi Wang, Han Yu, He Yan,
Ryan T. K. Kwok, Jianwei Sun, Le Li,* Haijun Ma,* Jacky W. Y. Lam,* and Ben Zhong Tang*

Cite This: https://doi.org/10.1021/acsnano.5c19751

Read Online

ACCESS | Metrics & More | Article Recommendations | Supporting Information

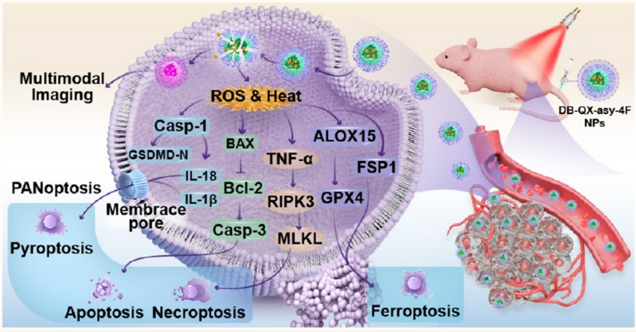

ABSTRACT: Phototheranostic strategies for cancer remain constrained by the availability of phototheranostic agents. Nonfullerene acceptor (NFA) materials, characterized by their distinctive structure and optical characteristics, emerge as promising candidates for the high-performance phototheranostic agents. In this work, an A−D−A′−D−A type NFA material (DB-QX-asy-4F) was designed as a phototheranostic agent to facilitate a comprehensive therapeutic effect on breast cancer by integrating the mechanisms of ferroptosis and PANoptosis. Briefly, the DB-QX-asy-4F and DSPE-mPEG-cRGD form biocompatible nanoparticles DB-QX-asy-4F NPs through self-assembly. Such NPs displayed strong emission fluorescence that redshifts to the NIR-II region, a large Stokes shift of 235 nm, and a quantum yield of 1.97%. Furthermore, DB-QX-asy-4F NPs enables the realization of precise tumor localization, high-resolution fluorescence imaging, photoacoustic imaging, and clear vascular imaging. These NPs generated both type I ($^{\bullet}O_2^{-}$, $^{\bullet}OH$) and type II ($^1O_2$) reactive oxygen species (ROS), and exhibited super photothermal conversion efficiency of 48.49%, endowing it with a synergistic photodynamic therapy (PDT)−photothermal therapy (PTT) capability to effectively suppressing tumor growth. Mechanistically, the therapeutic effects were mediated primarily through the regulation of ferroptosis and PANoptosis pathways. Overall, this system offers innovative insights for advancing the development of phototheranostic agent and enhancing the understanding of their underlying molecular mechanisms.

KEYWORDS: *Photodynamic therapy, Photothermal therapy, Multimodal imaging, Ferroptosis, PANoptosis, Cancer therapy*

■ INTRODUCTION

Phototheranostics is an emerging biomedical technology that seamlessly integrates diagnostic imaging with therapeutic functionality within a single nanoplatform. In recent years, it has attracted significant attention in the pursuit of precision cancer treatment, owing to its advantages of high selectivity, strong therapeutic efficacy, minimal invasiveness, and cost-effectiveness.[1−7] Unlike conventional treatment modalities, phototheranostics allow real-time tumor visualization and localized therapy, thereby greatly improving both precision and safety.[8−12] However, existing phototheranostic agents encounter persistent challenges, including suboptimal biocompatibility, complicated synthetic routes, limited tunability within the near-infrared (NIR) spectrum, and risks of long-term bioaccumulation that may lead to toxicity.[13−15] These limitations have driven the search for next-generation agents—particularly organic small molecules—with enhanced optical performance, excellent biosafety, and structurally tunable designs to meet the demands of advanced phototheranostic applications. Nonfullerene acceptors (NFAs), originally developed for organic photovoltaic (OPV) devices, have recently attracted attention as versatile phototheranostic agents due to their structural tunability and superior photothermal performance.[16−22] These molecules typically adopt donor−-acceptor−donor (D−A−D) or acceptor−donor−acceptor (A−D−A) architectures based on rigid fused aromatic backbones.[23−26] By fine-tuning end groups, conjugated cores, and side chains, NFAs can be engineered to exhibit strong intramolecular charge transfer (ICT), extending absorption into the second near-infrared window (NIR-II, 1000−1700 nm) and enhancing photothermal conversion, reactive oxygen species (ROS) generation, and photostability.[27−31] Such features make them suitable for photothermal therapy

Received: November 13, 2025
Revised: January 19, 2026
Accepted: January 22, 2026

Scheme 1. Mechanism Diagram of DB-QX-asy-4F NPs for Malignant Breast Cancer via Integrating Ferroptosis and PANoptosis[a]

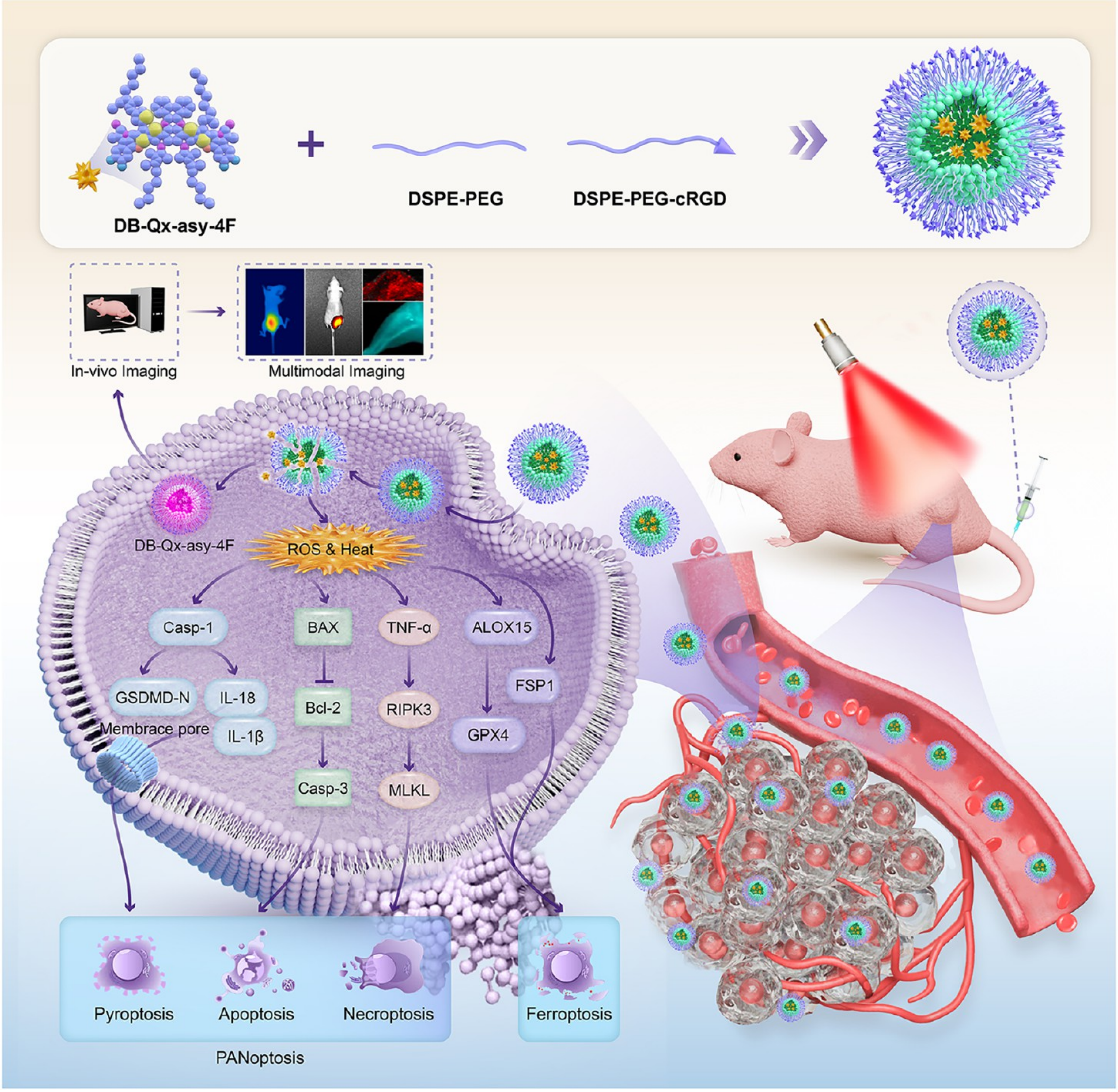

[a] The surface cRGD ligand specifically binds to integrin $\alpha v\beta 3$ (overexpressed on MDA-MB-231 cells), mediating targeted NP internalization to support ROS generation, photothermal effects, and activation of ferroptosis/PANoptosis pathways.

(PTT), photodynamic therapy (PDT), and fluorescence imaging (FLI), particularly in deep-tissue applications. Mechanistically, pronounced ICT enhances light absorption and ROS yield under laser excitation, while improving photothermal efficiency and intersystem crossing (ISC) through controlled molecular aggregation and optimized electronic structures.[32−35] These synergistic effects contribute to high photostability and robust therapeutic performance in physiological environments. Experimental studies further demonstrate that NFA-based phototheranostic systems can achieve precise tumor eradication, deep-tissue imaging, and targeted mitochondrial therapy, while maintaining excellent water dispersibility, biodegradability, and low systemic toxicity.[36,37]

Recent evidence suggests that phototheranostic agents can trigger not only classical apoptosis but also a spectrum of regulated cell death processes collectively termed PANoptosis, which includes necroptosis, pyroptosis, and other programmed pathways.[38−41] Among these, ferroptosis—an iron-dependent, nonapoptotic form of regulated cell death characterized by excessive lipid peroxidation—has drawn particular attention as a key contributor to phototheranostic efficacy.[42−45] Phototherapy induces ferroptosis either by generating excessive ROS or by disturbing intracellular iron homeostasis, leading to potent cytotoxicity. Importantly, the cooperative interaction between ferroptosis and PANoptotic pathways can amplify therapeutic outcomes while mitigating tumor resistance arising from evasion of a single death pathway.[46−48] Despite these advances, the molecular crosstalk between ferroptosis and PANoptosis in the context of NFA-based phototheranostics remains largely unexplored, and the specific signaling mechanisms involved have yet to be elucidated. Developing novel NFA-based systems capable of orchestrating multiple regulated cell death mechanisms—supported by comprehensive mechanistic studies—will be essential for optimizing phototherapeutic strategies and advancing them toward clinical application. To address this gap, we sought to design an integrated platform that not only enables precise imaging-

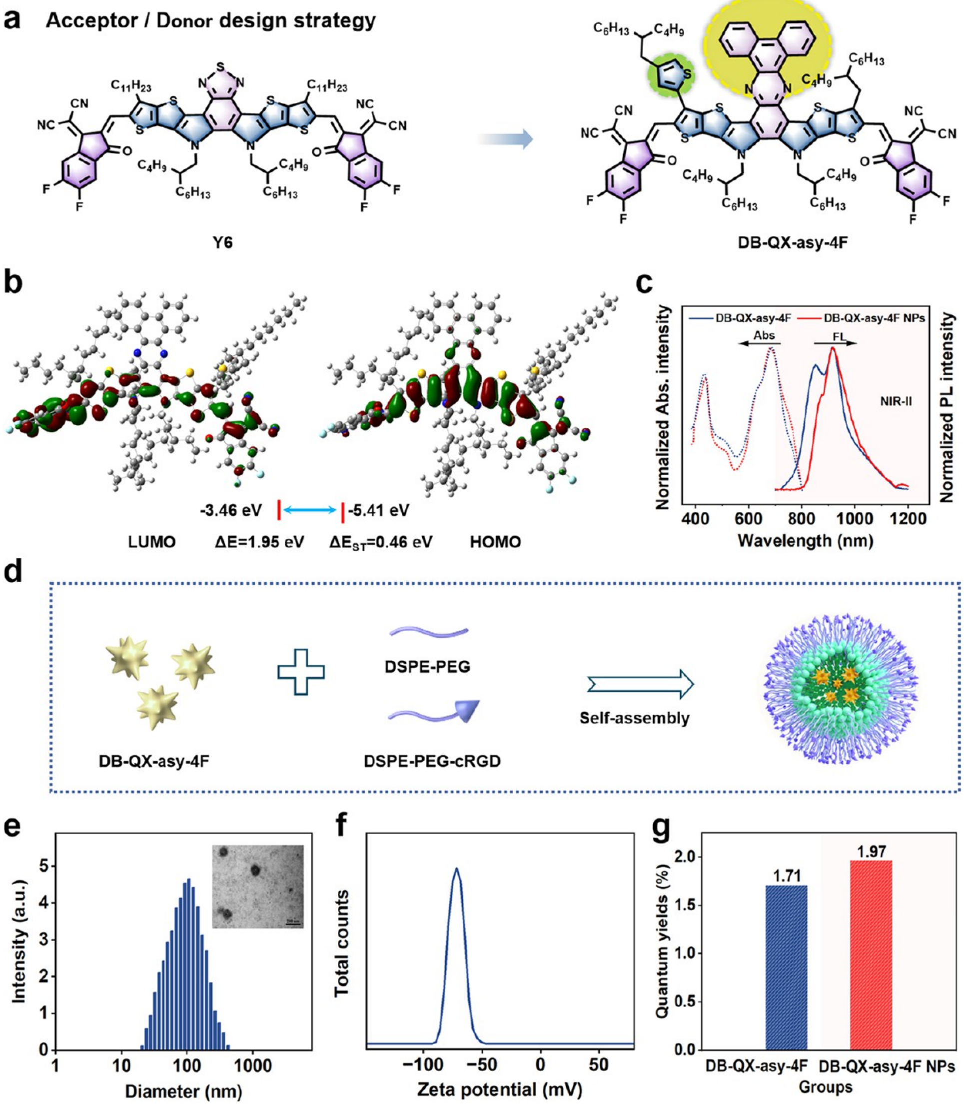

Figure 1. Molecular design and photophysical properties of DB-QX-asy-4F NPs. (a) Chemical structures of DB-QX-asy-4F and Qx acceptors. (b) Theoretical calculations of DB-QX-asy-4F. (c) Absorption and fluorescence spectra of DB-QX-asy-4F and NPs. (d) Schematic illustration of DB-QX-asy-4F NPs formulation. (e) Hydrodynamic diameter distribution and TEM image of DB-QX-asy-4F NPs (Scale bar: 100 nm). (f) ζ-potential analysis. (g) Quantum yield of DB-QX-asy-4F NPs (20 μM) in water under 635 nm laser irradiation (0.3 W·cm^{-2}).

guided therapy but also allows us to probe how NFA-based systems can engage distinct, yet interconnected, cell death programs. By embedding mechanistic exploration within the material design, we aimed to provide both functional therapeutic efficacy and new biological insights.

In this work, we developed a nonfullerene acceptor (NFA)-based phototheranostic material that integrates diagnostic and therapeutic functions. Serving as a versatile "Jack of All Trades," it enables multimodal imaging-guided PDT−PTT while simultaneously inducing ferroptosis and PANoptosis, thereby coordinating multiple cell death pathways and markedly enhancing antitumor efficacy (Scheme 1). Specifically, quinolinone (Qx), a core with relatively low electronegativity, was incorporated to construct DB-QX-asy-4F with an A−D−A′−D−A configuration. This innovative architecture replaces the conventional BTZ core to optimize energy level alignment and simplify synthesis, while integrating alkyl side chains and Y-shaped three-arm symmetry for enhanced biocompatibility and multifunctional integration (NIR-II emission, high PCE, and dual-type ROS generation) distinct from traditional D−A−D/A−D−A NFAs. Co-assembly of DB-QX-asy-4F with DSPE-mPEG-cRGD yielded biocompatible nanoparticles (DB-QX-asy-4F NPs), which exhibited strong NIR-II fluorescence, a large Stokes shift of 230 nm, and a quantum yield of 1.97%. Upon 635 nm laser irradiation, DB-QX-asy-4F induced rapid local heating and achieved a high photothermal conversion efficiency (PCE) of 48.49%, surpassing many reported NFA-based systems. Beyond thermal effects, light exposure triggered robust reactive oxygen species (ROS) generation. Both Type I ROS (superoxide anion $^{\bullet}O_2^-$ and hydroxyl radicals •OH) and Type II singlet oxygen ($^1O_2$) were efficiently produced, amplifying oxidative stress and creating a hostile intracellular environment conducive to regulated cell death. Mechanistic studies revealed strong activation of apoptosis, necroptosis, and pyroptosis, as evidenced by downregulation of Bcl-2, upregulation of Bax, Caspase-3 activation, TNF-α signaling, phosphorylation of RIPK3, MLKL activation, Caspase-1 cleavage, GSDMD-N formation, and release of pro-inflammatory cytokines IL-1β and IL-18. In parallel, ROS-induced lipid peroxidation initiated ferroptosis, as indicated by altered expression of GPX4, ALOX15, and FSP1. The interplay between ferroptosis and PANoptosis provided a multifaceted therapeutic strategy that effectively overcame the limitations of monomodal treatments. Taken together, these findings highlight the considerable potential of NFA-based materials as multifunctional phototheranostic agents. By combining deep-tissue NIR-II imaging, efficient photothermal performance, potent ROS generation, and coordinated activation of multiple cell death pathways, this study not only broadens the mechanistic understanding of NFA-mediated cancer therapy but also establishes a strong foundation for their further development and clinical translation in precision oncology.

RESULTS AND DISCUSSION

Molecular Design and Synthesis

Recent studies on Y6 have demonstrated that the benzothiadiazole (BTZ) acceptor unit plays a key role in promoting ICT and tuning energy levels.[49−52] Based on this understanding, quinolinone (Qx) with lower electronegativity was strategically selected as a core alternative in this study (Figure 1a). Compared with BTZ, the weaker electronegativity of the Qx core reduces the ICT effect and broadens the bandgap, while its stronger electron-donating characteristics elevate the HOMO and LUMO energy levels. This enhances electron injection capability and improves photothermal conversion efficiency, thereby endowing greater potential in photothermal therapy (PTT).[53−55] Additionally, the smaller energy level difference between donor and acceptor facilitates exciton dissociation and charge transfer, reducing energy loss and improving both photothermal performance and stability. Based on these considerations, an A−D−A′−D−A type nonfullerene acceptor (NFA) molecule was designed, featuring a quinolinone-derived acceptor core. The molecule adopts a Y-shaped three-armed symmetry, characterized by a strongly conjugated backbone and electron-withdrawing terminal groups. The design strategy focused on several aspects: first, a large π-conjugated central backbone was constructed using nitrogen-containing heterocycles, thiophene, and perylene units to achieve efficient light absorption, electron transport, and structural rigidity; second, alkyl side chains such as C_4H_9 and C_6H_{13} were introduced to enhance solubility and improve solution processability; third, strong electron-withdrawing groups including − CN, − F, and C═O were incorporated at the terminals to enhance electron affinity, induce red-shifted absorption, and modulate energy levels; finally, the Y-shaped three-arm symmetric structure was employed to broaden the absorption range and optimize molecular packing. Structural optimization was further achieved at the molecular level: conjugation between terminal aromatic rings and −CN or C═O groups strengthened electron-withdrawing capacity and ICT; thiophene units served as donor segments to form a highly conjugated main chain, improving electron delocalization, light absorption efficiency, and molecular planarity, thereby promoting π−π stacking and ordered packing to enhance material stability. Notably, the introduction of thiophene rings not only increased molecular rigidity, restricted internal rotation, and reduced nonradiative energy loss, but also facilitated tight packing and near-infrared absorption due to small steric hindrance, which is advantageous for deep-tissue therapy. Furthermore, this molecular architecture effectively promoted ISC, enhancing ROS generation and thereby improving the efficacy of photodynamic therapy (PDT).

Based on this design strategy, DB-QX-asy-4F was synthesized as illustrated in Figure S1 (Supporting Information), with detailed experimental procedures provided in the Experimental Methods section. The molecule adopts an A−D−A′−D−A conjugated architecture, in which electron-donating units alternate with two distinct types of electron-accepting units, forming a highly delocalized π-conjugated backbone. This structural arrangement endows the molecule with strong optical absorption and excellent photostability.[56,57] The successful synthesis of the target compound was confirmed by mass spectrometry (Figure S2) and nuclear magnetic resonance (NMR) spectroscopy (Figures S3−S7). Theoretical calculations indicated that the LUMO is predominantly localized on the acceptor units, while the HOMO is mainly distributed over the donor segments, revealing pronounced ICT character. The HOMO−LUMO energy gap was calculated to be 1.95 eV, and the singlet−triplet energy gap (ΔE_{ST}) was 0.46 eV, consistent with the electronic structure required for efficient light absorption, charge separation, and intersystem crossing, thus supporting enhanced photothermal and photodynamic performance. UV−vis absorption and fluorescence measurements revealed an absorption maximum at 685 nm, corresponding to the ICT transition, and an emission peak at 918 nm, confirming strong fluorescence and effective light-harvesting. These optical properties provide a solid foundation for the application of DB-QX-asy-4F in photothermal and photodynamic therapy.

Photophysical Properties of DB-QX-asy-4F NPs

The photophysical properties of DB-QX-asy-4F nanoparticles (NPs) are critical for their application in imaging and therapy. To enhance the biocompatibility and stability of these hydrophobic conjugated molecules in biological environments, and to achieve active targeting to MDA-MB-231 triple-negative breast cancer cells (overexpressing integrin $\alpha v\beta 3$), NPs were prepared using a one-step nanoprecipitation method with 1,2-distearoyl-sn-glycero-3-phosphoethanolamine-N-[methoxy (polyethylene glycol)] (DSPE-mPEG) and 1,2-Distearoyl-sn-glycero-3-phosphoethanolamine−polyethylene glycol−cyclic RGD peptide (DSPE-PEG-cRGD) (Figure 1d)—where the cyclic RGD (cRGD) moiety specifically binds to integrin $\alpha v\beta 3$ to facilitate targeted NP internalization, improve tumor-selective accumulation, and amplify the subsequent therapeutic effects. Dynamic light scattering (DLS) and transmission electron microscopy (TEM) analyses confirmed that DB-QX-asy-4F NPs exhibited uniform spherical morphology with an average hydrodynamic diameter of about 111.6 nm (Figure 1e). This size is favorable for passive tumor accumulation via the enhanced permeability and retention (EPR) effect. The stability of the DB-QX-asy-4F NPs was further evaluated. The ζ-potential was measured to be −71 mV (Figure 1f), indicating strong electrostatic repulsion that maintains good dispersion of the nanoparticles in solution. Long-term storage stability tests (Figure S8) showed that particle size remained unchanged with no precipitation after 10 days of storage in various solutions, demonstrating excellent stability. Subsequently, the key photophysical characteristics of DB-QX-asy-4F NPs, including absorption and emission spectra, quantum yield, and photostability, were systematically examined. The

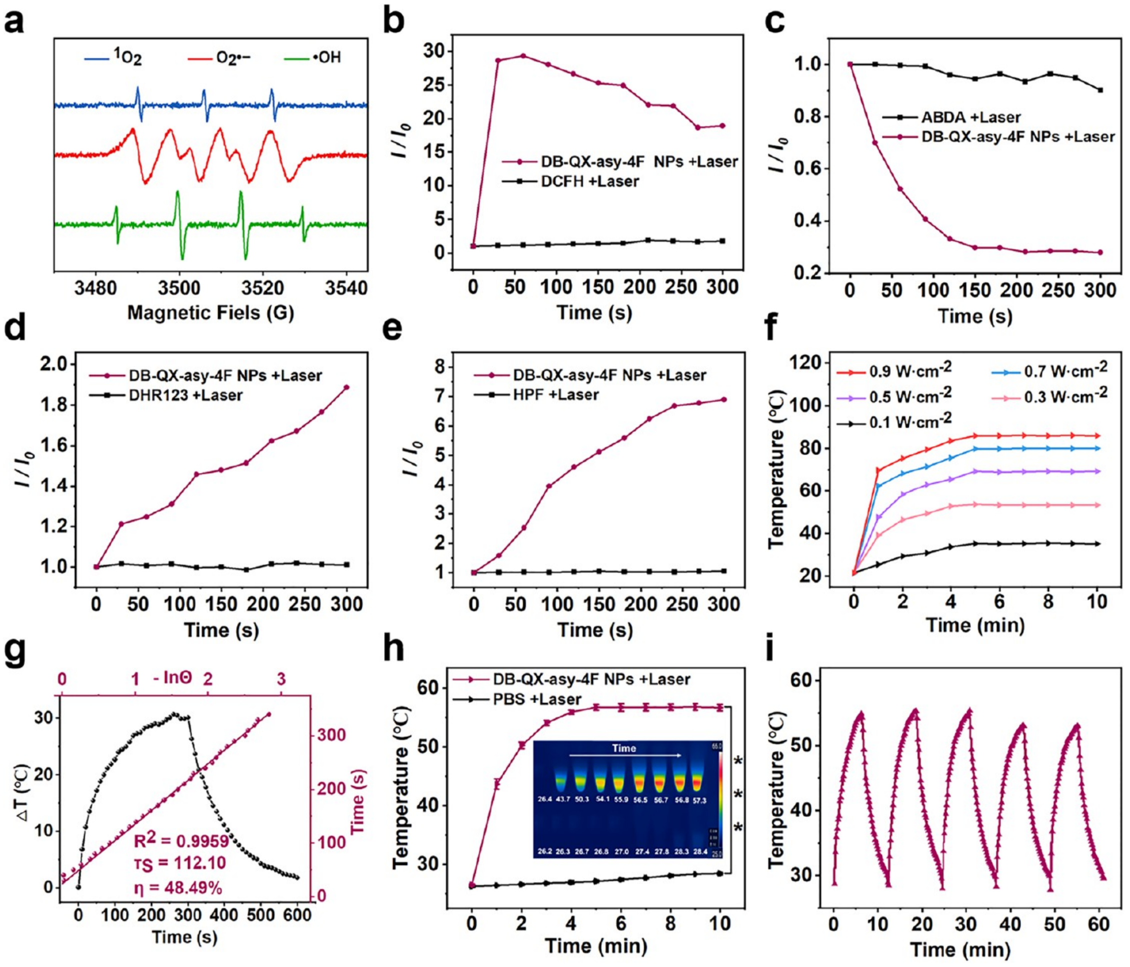

Figure 2. Capabilities of DB-QX-asy-4F NPs to generate ROS and produce heat. (a) ESR spectra showing singlet oxygen, hydroxyl radicals, and superoxide anions generated by DB-QX-asy-4F NPs under 635 nm laser irradiation for 10 min (b−e) ROS levels detected using DCFH-DA, ABDA, DHR123, and HPF probes. (f) Photostability of DB-QX-asy-4F NPs (20 μM) under continuous 635 nm laser irradiation at varying power intensities for 10 min (g) Photothermal conversion efficiency (PCE) of DB-QX-asy-4F NPs (20 μM) under 635 nm irradiation (0.3 W·cm^{-2}). (h) Photothermal stability of DB-QX-asy-4F NPs under continuous 635 nm irradiation (0.3 W·cm^{-2}) for 10 min (n = 3, $***p < 0.001$), with corresponding infrared thermal images. (i) Thermostability of DB-QX-asy-4F NPs under 635 nm irradiation (0.3 W·cm^{-2}) for five heating−cooling cycles.

absorption spectra revealed a pronounced peak in the near-infrared (NIR) region at 681 nm (Figure 1c), advantageous for deep-tissue imaging and photothermal applications. This strong absorption is attributed to the extended π-conjugation of the A−D−A′−D−A molecular framework, which enhances light harvesting. Emission spectra recorded under excitation at the absorption maximum displayed a distinct emission peak at 916 nm (Figure 1c) and extended into the near-infrared II (NIR-II) region. The corresponding Stokes shift of 235 nm indicated effective separation between absorption and emission processes, minimizing reabsorption losses. The photoluminescence quantum yield (Φ) was measured using the four-curve method, and the obtained value was 1.97% (Figure 1g). Such a relatively high yield enables effective photon conversion, thereby improving both the resolution and sensitivity of fluorescence imaging. As shown in Figure S9, fluorescence lifetime measurements in an organic solvent yielded a short lifetime of 0.43 ns, indicating rapid excited-state relaxation. Upon formation of nanoparticles, the lifetime increased to 1.74 ns, reflecting restricted molecular motion and enhanced intermolecular interactions that stabilize the excited state and promote efficient ROS generation and photothermal conversion. Collectively, these favorable photophysical properties highlight the strong potential of DB-QX-asy-4F NPs to improve photothermal performance and enable advanced biomedical applications.

ROS Generation and Heat Production by DB-QX-asy-4F NPs

To verify the photophysical properties, the ability of DB-QX-asy-4F NPs to generate reactive oxygen species (ROS), specifically singlet oxygen ($^1O_2$), hydroxyl radicals ($^\bullet OH$), and superoxide anion radicals ($^\bullet O_2^-$), was investigated using electron spin resonance (ESR) spectroscopy and fluorescence probe methods. The ESR spectra revealed pronounced signals corresponding to singlet oxygen and hydroxyl radicals generated upon irradiation (Figures 2a, and S10−S12). The characteristic peaks confirmed the presence of these reactive species, validating that DB-QX-asy-4F NPs are effectively activated under specific laser illumination. The results obtained from the fluorescence probe method were consistent with ESR spectroscopy, further confirming that DB-QX-asy-4F NPs effectively generated $^1O_2$, $^\bullet OH$, and $^\bullet O_2^-$ upon irradiation (Figures 2b−e and S13−S14). These results indicate that DB-

https://doi.org/10.1021/acsnano.5c19751

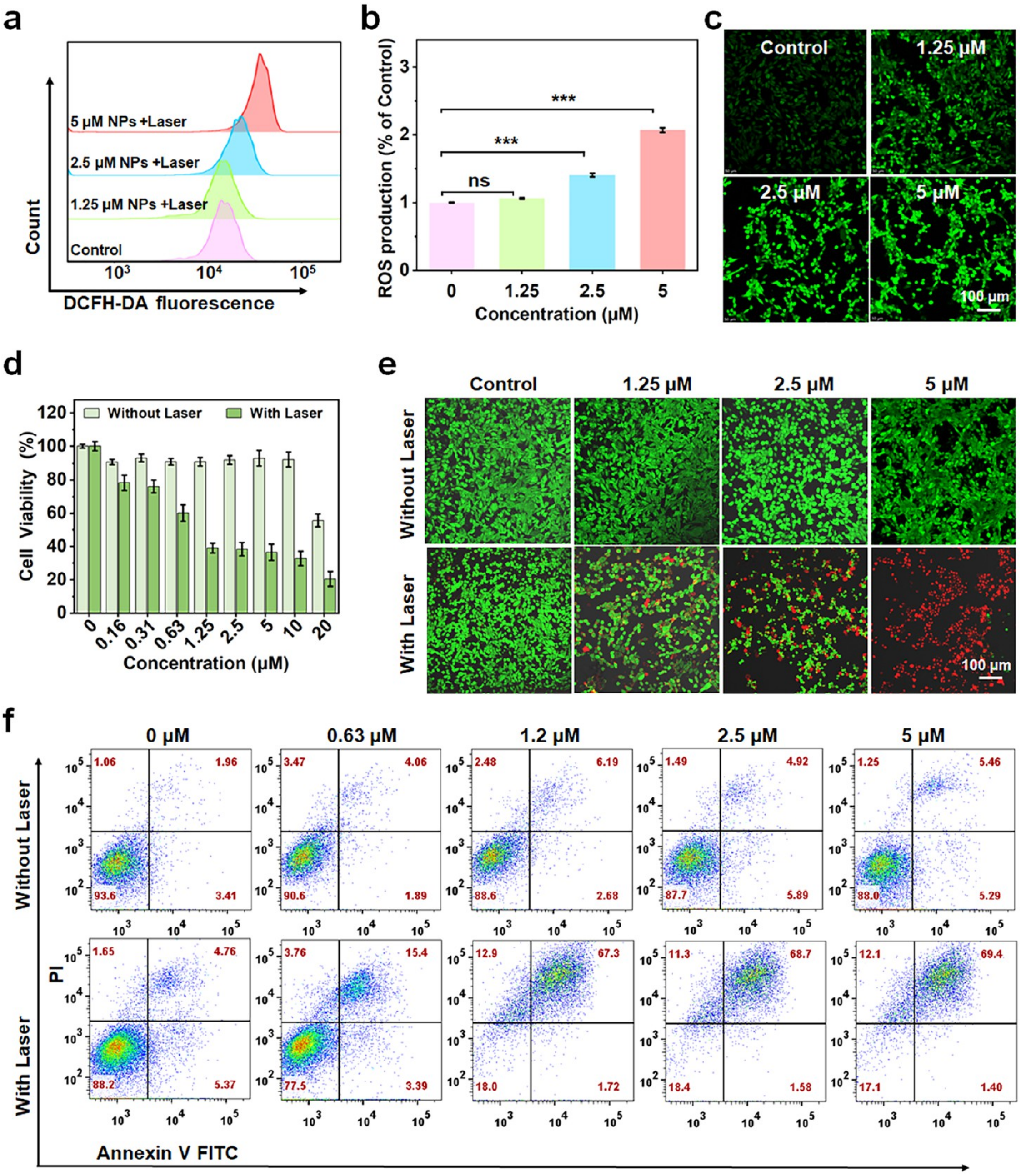

Figure 3. In vitro cytotoxicity of DB-QX-asy-4F NPs. (a) Intracellular ROS levels of MDA-MB-231 cells detected by flow cytometry and (b) quantitative analysis of results ($n = 3$, $***p < 0.001$). (c) Intracellular ROS levels of MDA-MB-231 cells detected by laser scanning confocal microscopy (Scale bar: 100 μm). (d) Viability of MDA-MB-231 cells incubated with DB-QX-asy-4F NPs at varying concentrations with or without 635 nm laser irradiation for 10 min (0.3 W·cm^{-2}) ($n = 3$, $***p < 0.001$). (e) Live/dead cell staining of MDA-MB-231 cells treated with DB-QX-asy-4F NPs using Calcein-AM/PI (Scale bar: 100 μm). (f) Induction of apoptosis assessed through flow cytometry.

QX-asy-4F NPs are capable of generating both type I and type II reactive oxygen species. To evaluate photothermal conversion performance, solutions of DB-QX-asy-4F NPs at different concentrations were exposed to 635 nm laser irradiation at varying power levels. Temperature changes were monitored in real time by controlling the irradiation time (Figure 2f and S15). The results demonstrated that with increasing laser power, the temperatures of DB-QX-asy-4F NPs at concentrations of 10 μM and 20 μM both rose significantly, confirming their excellent photothermal conversion ability. Notably, under the same laser power, the 20 μM NP solution exhibited a more pronounced temperature elevation compared to the 10 μM group. Specifically, after 4 min of exposure, the temperature of the 20 μM solution reached 57 °C (Figure 2h), while the 10 μM solution showed a lower temperature rise (detailed data in Figure S15), further verifying that the photothermal conversion capability of DB-QX-asy-4F NPs is concentration-dependent under the same power condition. The photothermal conversion efficiency of the NPs was calculated as 48.49% (Figure 2g). Additionally, DB-QX-asy-4F NPs are able to undergo multiple photothermal cycles without a significant decrease in temperature during subsequent cycles compared to the first cycle (Figure 2i). This stability is crucial for long-term imaging applications and ensures reliable

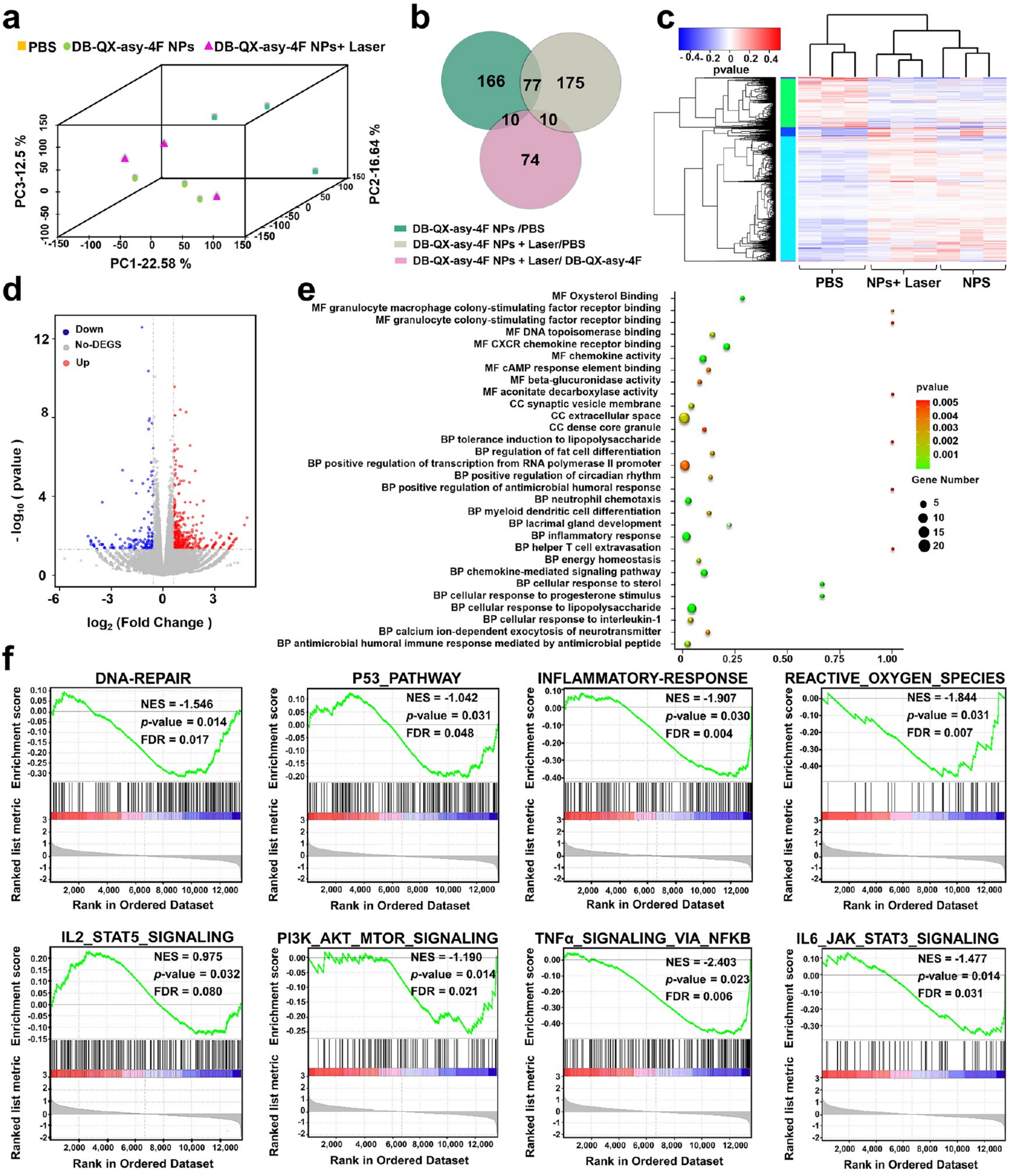

Figure 4. RNA sequencing analysis results. (a) Principal Component Analysis (PCA) plot. (b) Venn diagram of differential genes. (c) Heatmap of differential gene clustering. (d) Volcano plot of differential genes (red: upregulated; blue: downregulated). (e) GO enrichment scatter plot. (f) GSEA enrichment analysis of transcriptomic data for DB-QX-asy-4F NPs + Laser treated breast cancer cells.

performance across different environments. Overall, the photophysical properties of the DB-QX-asy-4F NPs—including strong NIR absorption, robust type I ROS generation, high quantum yield, and excellent photostability—highlight their suitability for multimodal imaging and photothermal therapy.

Phototherapy Effect Evaluation of DB-QX-asy-4F NPs In Vitro

The phototherapy effect of DB-QX-asy-4F NPs was evaluated using the MDA-MB-231 triple-negative breast cancer cell line as a representative model. Cell viability was first determined

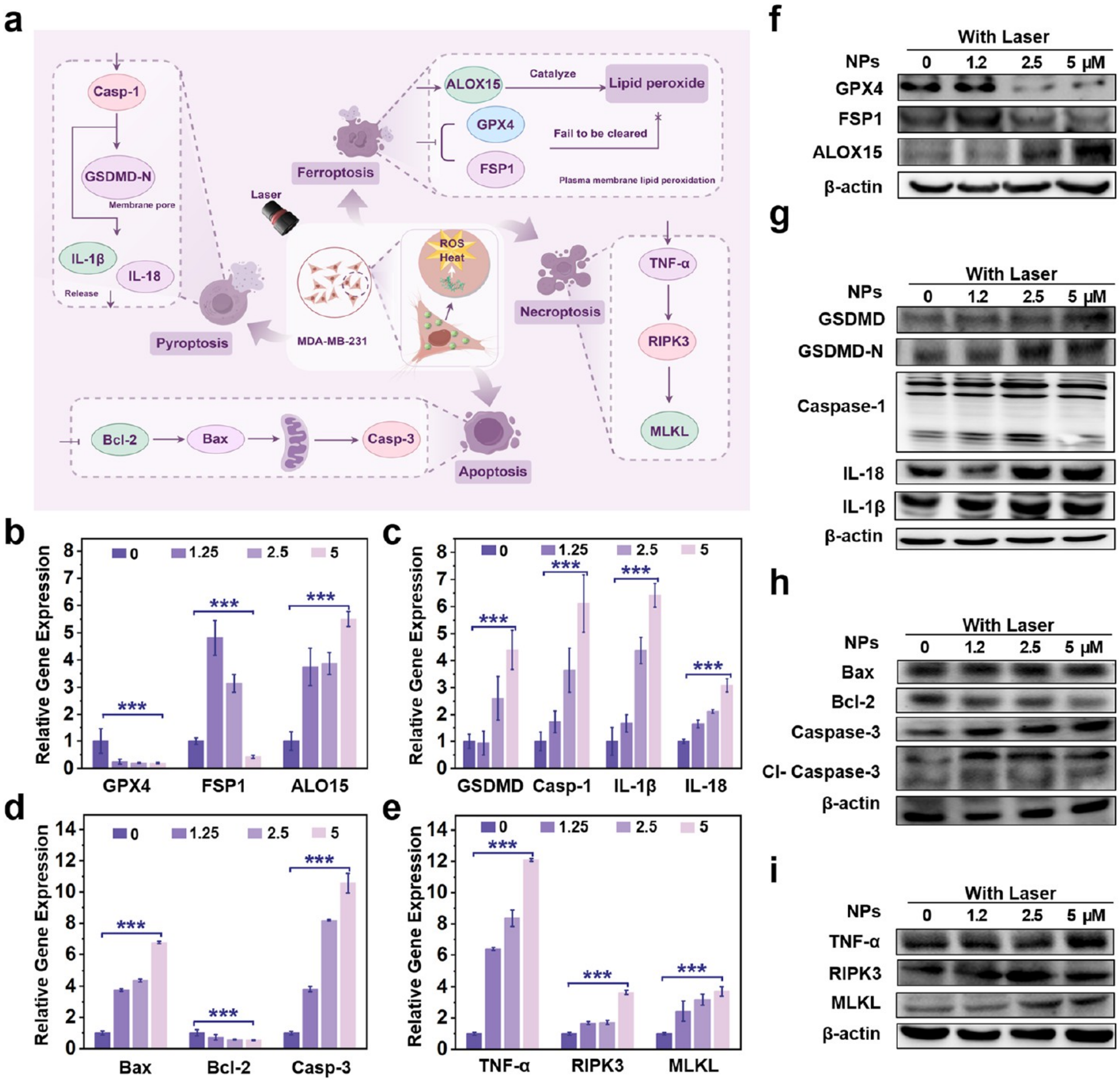

Figure 5. Cytocidal mechanism of DB-QX-asy-4F NPs + Laser treatment on breast cancer cells. (a) Molecular mechanism diagram. (b−e) q-PCR analysis of changes in expression of genes related to ferroptosis (b), pyroptosis (c), apoptosis (d), and necroptosis (e). (f−i) Western blot analysis of protein expression related to ferroptosis (f), pyroptosis (g), apoptosis (h), and necroptosis (i).

using the Cell Counting Kit-8 (CCK-8) assay to assess dark toxicity (Figures S16 and 3d). In the absence of laser irradiation, DB-QX-asy-4F NPs exhibited negligible cytotoxicity after 12 h of incubation, with cell viability remaining above 80% at concentrations below 10 μM, indicating low toxicity and excellent biocompatibility under dark conditions. This ensures that the NPs are activated only under laser exposure, minimizing side effects on healthy tissues. Intracellular ROS levels were quantified using flow cytometry and visualized with laser scanning confocal microscopy (Figure 3a−c). The results revealed a concentration-dependent increase in intracellular ROS following NPs treatment, further supporting their high efficacy in killing cancer cells through synergistic PDT and PTT mechanisms. Subsequently, the photodynamic and photothermal therapeutic effects were evaluated under 635 nm NIR laser irradiation (Figures 3d and S17). DB-QX-asy-4F NPs demonstrated significant cytotoxicity across all tested cancer cell lines. In a dose-dependent manner, MDA-MB-231 cell viability dropped below 43% at a concentration of 0.63 μM with a laser power density of 0.3 W·cm^{-2}. A similar trend was observed in other cancer cell lines (4T1 and HCT116), supporting the broad applicability of this material (Figures S18−S19). Live/dead staining assays provided visual confirmation of the cancer-cell-killing effect (Figure 3e). After irradiation, cells treated with DB-QX-asy-4F NPs exhibited strong red fluorescence (dead cells), whereas the untreated control group predominantly showed green fluorescence (live cells). Flow cytometry analysis using Annexin V/propidium iodide (PI) staining was conducted to differentiate apoptosis from necrosis (Figure 3f). The results showed a high percentage of apoptotic cells after treatment, confirming that ROS generated by the NPs primarily induced apoptosis. Additionally, the photothermal effect contributed to cell membrane disruption, leading to necrotic cell death in some cases. These in vitro studies demonstrate that DB-QX-asy-4F NPs possess strong phototherapy effect, with minimal dark toxicity and pronounced phototoxicity under NIR laser irradiation. The combination of ROS production and photothermal conversion provides a potent dual therapeutic approach for eliminating cancer cells, making DB-QX-asy-4F NPs a promising candidate for in vivo studies and future clinical translation.

https://doi.org/10.1021/acsnano.5c19751
ACS Nano XXXX, XXX, XXX−XXX

RNA Sequencing

To explore the molecular mechanisms underlying the phototherapy effect of DB-QX-asy-4F NPs on breast cancer cells, an in-depth transcriptomic analysis was performed before and after DB-QX-asy-4F NPs + Laser treatment using RNA sequencing. In the PCA plot (Figure 4a), samples from different treatment groups were clearly separated, indicating that DB-QX-asy-4F NPs + Laser significantly altered the transcriptomic landscape of breast cancer cells and exerted effects through specific biological pathways. Further analysis based on the Venn diagram indicated that PBS, DB-QX-asy-4F NPs and DB-QX-asy-4F NPs+ Laser contained 262, 253, and 94 genes, respectively. A total of 77 genes were shared between DB-QX-asy-4F NPs and PBS, reflecting a relatively high degree of similarity between these two groups. In contrast, DB-QX-asy-4F NPs+ Laser shared only 10 genes with either DB-QX-asy-4F NPs or PBS, while 74 genes were unique to this group, accounting for approximately 79% of its total and highlighting its distinctiveness. Taken together, these findings suggest that DB-QX-asy-4F NPs and PBS are more closely related, whereas DB-QX-asy-4F NPs+ Laser represents a comparatively independent group (Figure 4b). Differential expression analysis revealed 356 upregulated and 157 downregulated genes in the DB-QX-asy-4F NPs + Laser group compared with the control group (Figure 4c). The differential gene clustering heatmap further illustrated significant changes in gene expression patterns between the treated and control groups (Figure 4d). GO enrichment analysis visualized the functional classification of differentially expressed genes after DB-QX-asy-4F NPs + Laser treatment (Figure 4e). The scatter plot showed that the differentially expressed genes were primarily concentrated in biological processes such as oxidative stress response, inflammatory response, apoptosis, and immune response. Enriched molecular functions and cellular components were also identified, suggesting that DB-QX-asy-4F NPs + Laser eradicates breast cancer cells by modulating these biological processes. KEGG pathway enrichment analysis revealed that DB-QX-asy-4F NPs + Laser treatment significantly impacted tumor-associated signaling pathways, such as lipid peroxidation and chemokine (Figure S20). These alterations may contribute to the antitumor effects of the treatment. GSEA analysis further demonstrated that DB-QX-asy-4F NPs + Laser treatment affected pathways related to cancer progression and cell death (Figure 4f). The DNA repair pathway was downregulated, indicating impairment of DNA damage response, while the p53 pathway was enriched, suggesting activation of tumor suppressor mechanisms and potential cell cycle arrest and apoptosis. Negative enrichment of the adipogenesis pathway indicated metabolic reprogramming, while activation of the ROS pathway highlighted increased oxidative stress, likely driving ferroptosis and other cell death mechanisms. Additionally, TNF-α signaling via PI3k and other inflammatory pathways was activated, suggesting enhanced immune responses. These findings indicate that DB-QX-asy-4F NPs + Laser treatment significantly alters the transcriptomic profile of breast cancer cells by regulating genes involved in oxidative stress, inflammation, apoptosis, and immune responses, as well as by affecting tumor-associated signaling pathways.

Molecular Mechanistic Evaluation of the Phototherapeutic Effects

Based on predictive analysis, the cytotoxic mechanisms of DB-QX-asy-4F NPs combined with laser irradiation on breast cancer cells were experimentally validated. Transmission electron microscopy (TEM) revealed pronounced morphological alterations in breast cancer cells following DB-QX-asy-4F NPs combined with laser treatment (Figure S21). Notable features included mild chromatin condensation and partial loss, indicative of apoptotic signaling; mitochondrial shrinkage, and swelling, which are characteristic of ferroptosis and mitochondrial stress; cytoplasmic densification reflecting overall cellular stress and organelle compaction; and discontinuities, perforations, and blebbing in the plasma membrane, consistent with necroptotic and pyroptotic processes. Collectively, these ultrastructural changes provide compelling visual evidence for the concurrent activation of multiple regulated cell death pathways, including necroptosis, pyroptosis, and ferroptosis, in response to the phototheranostic treatment. Quantitative PCR (qPCR) was conducted to evaluate the expression of genes involved in apoptosis, necroptosis, pyroptosis, and ferroptosis (Figure 5b−e). Following treatment, necroptosis- and apoptosis-related genes, including TNF-α, RIPK3, MLKL, Caspase-3, and Bax, were significantly upregulated, while the antiapoptotic gene Bcl-2 was markedly downregulated, indicating strong activation of apoptotic pathways. Concurrently, pyroptosis markers—Caspase-1, GSDMD-N, IL-1β, and IL-18—were robustly upregulated, confirming induction of pyroptotic processes. Ferroptosis-associated genes were similarly modulated: ALOX15 expression increased significantly, whereas GPX4 and FSP1 were downregulated, demonstrating activation of ferroptotic pathways. Moreover, these transcriptional changes exhibited a clear dose-dependent pattern across increasing concentrations of DB-QX-asy-4F NPs (0, 1.25, 2.5, and 5 μM), suggesting that higher NPs doses amplify the activation of multiple regulated cell death pathways. Western blot analysis further corroborated these findings at the protein level (Figure 5f−i). Dose-dependent changes were observed for key cell death regulators: proapoptotic proteins Caspase-3 and Bax were progressively upregulated, while antiapoptotic Bcl-2 decreased, indicating robust apoptotic activation. Pyroptosis-related proteins, including Caspase-1, GSDMD-N, IL-1β, and IL-18, displayed marked concentration-dependent increases, confirming pyroptotic engagement. Concurrently, ferroptosis-associated proteins were significantly modulated: GPX4 and FSP1 levels progressively decreased, whereas ALOX15 was substantially elevated, reinforcing ferroptotic activation. Taken together, these results provide comprehensive molecular evidence that DB-QX-asy-4F NPs, under laser irradiation, coordinately induce apoptosis, necroptosis, pyroptosis, and ferroptosis in a dose-dependent manner. Integration of morphological, gene expression, and protein expression analyses confirms that this treatment exerts potent cytotoxic effects on breast cancer cells through the simultaneous activation of multiple programmed cell death pathways, offering a multifaceted strategy to overcome tumor resistance and enhance antitumor efficacy.

In Vivo NIR-II Fluorescence, Photoacoustic, and Body Vascular Imaging

To evaluate the real-time imaging capabilities of DB-QX-asy-4F NPs in a living system, in vivo imaging was performed using a mouse tumor model, including NIR-I/II fluorescence

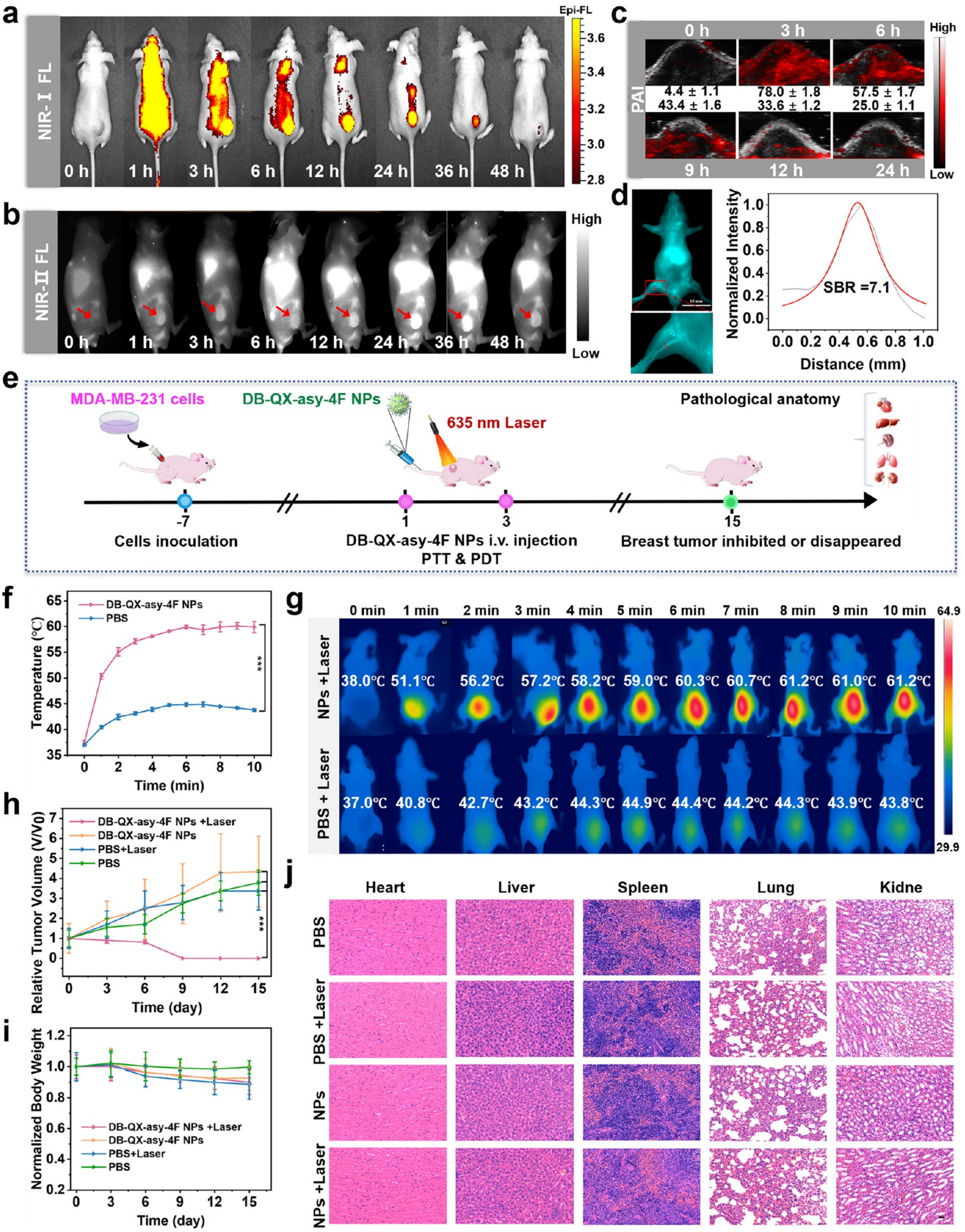

Figure 6. In vivo imaging and phototherapy. (a) NIR-I fluorescence images. (b) NIR-II fluorescence images. (c) Temporal evolution of photoacoustic signals. (d) Body vascular imaging. (e) Schematic illustration of in vivo phototherapy (with a dosage of 1.8 mg kg^{-1} body weight). (f) Temperature variations and (g) infrared thermal images of tumors following PBS and DB-QX-asy-4F NPs injection under 635 nm laser irradiation (0.3 W·cm^{-2}), recorded at different intervals ($n = 3$, $^{***}p < 0.001$). (h) Tumor volume changes for different treatment groups ($n = 6$,

Figure 6. continued

$^{***}p < 0.001$). (i) Body weight changes for different treatment groups ($n = 6$, $^{***}p < 0.001$). (j) H&E staining analysis of tissues after different treatments. Scale bar: 200 μm.

imaging, photoacoustic imaging and whole-body vascular imaging. Multiple imaging techniques were applied to comprehensively evaluate nanoparticle distribution and imaging performance in biological environments. Biosafety was first evaluated by hemolysis assays (Figure S22). At concentrations up to 20 μM, the hemolysis ratio remained consistently below the commonly accepted safety threshold of 5%. These observations suggest that the nanoparticles did not cause significant disruption of red blood cell (RBC) membranes, thereby demonstrating excellent hemocompatibility. Mice bearing subcutaneous tumors were injected with DB-QX-asy-4F NPs via tail vein administration. As shown in the NIR-I imaging results (Figures 6a and S23), strong fluorescence signals were observed in the tumor region, reaching a plateau between 12 and 24 h. Further imaging results (Figure 6b) demonstrated that fluorescence signals in the tumor peaked at 24 h, confirming efficient tumor accumulation via the EPR effect. This selective accumulation is critical for maximizing therapeutic efficacy while minimizing off-target effects. The high NIR-II fluorescence signal enabled clear visualization of the tumor site, highlighting the superior imaging depth and resolution of DB-QX-asy-4F NPs in the NIR-II window. The prolonged tumor retention also indicated their potential for long-term imaging and therapeutic monitoring. To investigate the time-resolved dynamics of photoacoustic signals after DB-QX-asy-4F NPs administration, tumor-region imaging was conducted at 0, 3, 6, 9, 12, and 24 h postinjection (Figure 6c). The signal intensity increased sharply from a baseline of 4.4 ± 1.1 arb. units to 78.0 ± 1.8 arb. units within 3 h—a 16.7-fold rise. This peak phase at 3 h formed a distinct plateau, with signal intensities significantly higher than at other time points. Beyond 6 h, the signal declined but remained elevated at 24 h (5.6-fold above baseline). Nonlinear regression analysis (R^2 = 0.998) defined a stable high-intensity window between 1−3 h, during which signal levels consistently exceeded 80% of the peak (Figure S24). These findings provide a robust, quantitative basis for identifying the optimal imaging window in preclinical and translational applications of DB-QX-asy-4F-mediated photoacoustic imaging. Whole-body vascular imaging demonstrated the distribution of nanoparticles in the vascular system, confirming their excellent blood circulation stability (Figure 4d). DB-QX-asy-4F enabled high-resolution visualization of the vascular network structure in the hind limbs, clearly revealing the morphology and distribution characteristics of blood vessels. With a signal-to-noise ratio of 7.1, the imaging clarity and contrast were significantly enhanced, allowing precise analysis of the vascular microenvironment and nanoparticle dynamics. In vivo NIR-II fluorescence, photoacoustic, and whole-body vascular imaging results demonstrated that DB-QX-asy-4F NPs exhibit strong tumor-targeting capability and excellent high-contrast imaging performance. These complementary imaging modalities enhance the accuracy and spatial resolution of tumor identification, enabling precise visualization of tumor distribution. Furthermore, the NPs displayed good stability and biocompatibility in vivo, ensuring persistent signals and safety during imaging. These advantages provide a solid foundation for early tumor diagnosis, real-time monitoring, and evaluation of therapeutic efficacy, underscoring their broad potential for clinical applications.

In Vivo Photodynamic and Photothermal Therapy

To assess the therapeutic efficacy of DB-QX-asy-4F NPs in vivo, experiments were conducted using a mouse tumor model (Figure 6e). The objective was to evaluate how these NPs jointly exert PDT and PTT effects under near-infrared (NIR) laser irradiation to achieve effective tumor treatment. Mice were divided into four groups: (1) PBS group, (2) PBS with laser irradiation, (3) DB-QX-asy-4F NPs without laser irradiation, and (4) DB-QX-asy-4F NPs with NIR laser irradiation. DB-QX-asy-4F NPs were administered via tail vein injection, followed by NIR laser irradiation (wavelength: 635 nm, power density: 0.3 W·cm^{-2}) for 10 min, with multiple treatments conducted at 2-day intervals. To further investigate the photothermal properties of DB-QX-asy-4F NPs in vivo, IR thermal imaging was performed. Following NIR laser irradiation at the tumor site (wavelength: 635 nm, power density: 0.3 W·cm^{-2}), tumor temperature was monitored in real time using an IR thermal camera (Figure 6f,g). In the DB-QX-asy-4F NPs treated group, tumor temperature increased rapidly, reaching ∼61 °C within 10 min, whereas the control group exhibited negligible temperature changes. The rapid and significant temperature rise confirmed the efficient photothermal conversion ability of the NPs, sufficient to induce hyperthermia for tumor ablation. Importantly, no excessive temperature elevation was detected in surrounding healthy tissues, demonstrating the localized heating effect of the NPs. To assess the therapeutic effect, tumor volumes were regularly measured using calipers, and growth curves were plotted (Figure 6h). The results showed a significant reduction in tumor growth in the group receiving both NPs and NIR laser irradiation, while the control group and the groups treated with only DB-QX-asy-4F NPs or laser irradiation exhibited rapid tumor growth (Figure S25). This indicates that the combined effects of photodynamic therapy and photothermal therapy effectively inhibited tumor progression. Throughout the treatment, the body weight and health status of the mice were continuously monitored. No significant weight loss or adverse reactions were observed, confirming that NPs treatment was safe and well-tolerated (Figure 6i). At the end of the experiment, tissues including heart, liver, spleen, lung, and kidney were collected for histological analysis (Figure 6j). Hematoxylin and Eosin (H&E) staining revealed no signs of pathological changes, further validating the therapeutic potential and biological safety of DB-QX-asy-4F NPs. The results from the in vivo photodynamic and photothermal therapy experiments demonstrated that DB-QX-asy-4F NPs effectively induced tumor cell death under near-infrared laser irradiation, showing strong therapeutic potential. This combination therapy not only enhanced treatment efficacy but also reduced side effects on healthy tissues, providing a novel strategy for cancer treatment. Future studies will further explore the clinical application potential and long-term effects of this therapy.

CONCLUSIONS

In summary, we successfully developed a nonfullerene acceptor (NFA)-based integrated phototheranostic platform, which seamlessly combines diagnostic and therapeutic functionalities within a single multifunctional system, demonstrating the versatility of a "Jack of All Trades." We designed and synthesized the A−D−A′−D−A structured molecule DB-QX-asy-4F, in which a quinoline unit with lower electronegativity replaces the conventional BTZ core, optimizing charge distribution, energy level alignment, and photophysical properties at the molecular level. Through self-assembly with DSPE-mPEG-cRGD, DB-QX-asy-4F forms nanoparticles (DB-QX-asy-4F NPs) with excellent aqueous solubility, colloidal stability, biocompatibility, and tumor-targeting capability—key properties that lay a solid foundation for its clinical translation. Functionally, DB-QX-asy-4F NPs exhibit remarkable near-infrared II (NIR-II) fluorescence emission, enabling high-resolution imaging of deep tissues. They also display high photothermal conversion efficiency and strong photosensitizing activity, allowing simultaneous generation of reactive oxygen species (ROS, both type I and type II) and effective photothermal effects under light irradiation. The synergistic combination of photodynamic therapy (PDT) and photothermal therapy (PTT) not only significantly enhances tumor ablation efficiency but also provides robust support for image-guided precision treatment. Mechanistically, this platform pioneers the synergistic activation of ferroptosis and PANoptosis (apoptosis/necroptosis/pyroptosis) in NFA-based phototheranostics. Ferroptosis is driven by ROS-induced lipid peroxidation, mediated by downregulated GPX4 and upregulated ALOX15; PANoptosis is activated via modulated expression of key regulators (e.g., Caspase-3, RIPK3, GSDMD-N). Their crosstalk overcomes tumor resistance from single-cell death pathway evasion, achieving comprehensive and irreversible tumor eradication.[58−60] In vivo studies confirm potent antitumor efficacy with negligible systemic toxicity, as evidenced by inhibited tumor growth, stable mouse body weight, and normal histology of major organs. Beyond these immediate findings, this work provides a conceptual framework for the rational design of next-generation NFA-based phototheranostic agents. The demonstrated ability to simultaneously combine deep-tissue imaging, efficient photothermal conversion, and multipathway cell death induction highlights the potential for tailored, patient-specific cancer therapies. Looking forward, further optimization of NFA structures, surface modifications for targeted delivery, and exploration of combination regimens with immunotherapies or chemotherapies could extend the therapeutic utility of this platform. Ultimately, the insights gained from DB-QX-asy-4F NPs not only deepen our mechanistic understanding of multimodal phototherapy but also pave the way for the development of clinically translatable, precision oncology strategies that maximize antitumor efficacy while minimizing off-target effects.

EXPERIMENTAL METHODS

Materials and Instrumentation, Synthesis and characterization of the target compounds were referred to Supporting Information. All animals are purchased from GemPharmatech, and all procedures were performed in accordance with the ethical guidelines established by the laboratory animal research center of Ningxia University (Animal Welfare Assurance no. NXU2025057, Ningxia, China).

ASSOCIATED CONTENT

Supporting Information

The Supporting Information is available free of charge at https://pubs.acs.org/doi/10.1021/acsnano.5c19751.

> Synthesis and structural characterization, including NMR and MS spectra of DB-QX-asy-4F; DFT calculation; fluorescence lifetime; photothermal conversion performance and ROS generation and stability of DB-QX-asy-4F NPs; Western blotting analysis, q-PCR analysis, cell imaging and in vivo imaging and therapy (PDF)

AUTHOR INFORMATION

Corresponding Authors

Le Li − *Key Lab of Ministry of Education for Protection and Utilization of Special Biological Resources in Western China, School of Life Sciences, Ningxia University, Yinchuan 750021, China*; Email: leli@nxu.edu.cn

Haijun Ma − *Key Lab of Ministry of Education for Protection and Utilization of Special Biological Resources in Western China, School of Life Sciences, Ningxia University, Yinchuan 750021, China*; orcid.org/0009-0007-1247-6670; Email: mahj@nxu.edu.cn

Jacky W. Y. Lam − *Department of Chemistry, the Hong Kong Branch of Chinese National Engineering Research Center for Tissue Restoration and Reconstruction, State Key Laboratory of Nervous System Disorders, and Department of Chemical and Biological Engineering, The Hong Kong University of Science and Technology, Kowloon, Hong Kong 999077, China*; Email: chjacky@ust.hk

Ben Zhong Tang − *Department of Chemistry, the Hong Kong Branch of Chinese National Engineering Research Center for Tissue Restoration and Reconstruction, State Key Laboratory of Nervous System Disorders, and Department of Chemical and Biological Engineering, The Hong Kong University of Science and Technology, Kowloon, Hong Kong 999077, China; Guangdong Basic Research Center of Excellence for Aggregate Science, School of Science and Engineering, The Chinese University of Hong Kong (Shenzhen), Shenzhen, Guangdong 518172, China*; orcid.org/0000-0002-0293-964X; Email: tangbenz@cuhk.edu.cn

Authors

Xiaoli Lu − *Key Lab of Ministry of Education for Protection and Utilization of Special Biological Resources in Western China, School of Life Sciences, Ningxia University, Yinchuan 750021, China; School of Laboratory Medicine, Ningxia Medical University, Yinchuan 750004, China*

Lan Xie − *Department of Chemistry, the Hong Kong Branch of Chinese National Engineering Research Center for Tissue Restoration and Reconstruction, State Key Laboratory of Nervous System Disorders, and Department of Chemical and Biological Engineering, The Hong Kong University of Science and Technology, Kowloon, Hong Kong 999077, China*

Huan Yu − *Department of Radiation Oncology, General Hospital of Ningxia Medical University, Yinchuan 750004, China*

Yunfei Zuo − *Department of Chemistry, the Hong Kong Branch of Chinese National Engineering Research Center for Tissue Restoration and Reconstruction, State Key Laboratory of Nervous System Disorders, and Department of Chemical* *and Biological Engineering, The Hong Kong University of Science and Technology, Kowloon, Hong Kong 999077, China*

Guokang He − *Department of Chemistry, the Hong Kong Branch of Chinese National Engineering Research Center for Tissue Restoration and Reconstruction, State Key Laboratory of Nervous System Disorders, and Department of Chemical and Biological Engineering, The Hong Kong University of Science and Technology, Kowloon, Hong Kong 999077, China*

Jinyi Wang − *Department of Chemistry, the Hong Kong Branch of Chinese National Engineering Research Center for Tissue Restoration and Reconstruction, State Key Laboratory of Nervous System Disorders, and Department of Chemical and Biological Engineering, The Hong Kong University of Science and Technology, Kowloon, Hong Kong 999077, China*

Han Yu − *Department of Applied Biology and Chemical Technology and Research Institute for Smart Energy, The Hong Kong Polytechnic University, Kowloon, Hong Kong 999077, China;* orcid.org/0000-0003-1936-5328

He Yan − *Department of Chemistry, the Hong Kong Branch of Chinese National Engineering Research Center for Tissue Restoration and Reconstruction, State Key Laboratory of Nervous System Disorders, and Department of Chemical and Biological Engineering, The Hong Kong University of Science and Technology, Kowloon, Hong Kong 999077, China;* orcid.org/0000-0003-1780-8308

Ryan T. K. Kwok − *Department of Chemistry, the Hong Kong Branch of Chinese National Engineering Research Center for Tissue Restoration and Reconstruction, State Key Laboratory of Nervous System Disorders, and Department of Chemical and Biological Engineering, The Hong Kong University of Science and Technology, Kowloon, Hong Kong 999077, China;* orcid.org/0000-0002-6866-3877

Jianwei Sun − *Department of Chemistry, the Hong Kong Branch of Chinese National Engineering Research Center for Tissue Restoration and Reconstruction, State Key Laboratory of Nervous System Disorders, and Department of Chemical and Biological Engineering, The Hong Kong University of Science and Technology, Kowloon, Hong Kong 999077, China;* orcid.org/0000-0002-2470-1077

Complete contact information is available at:
https://pubs.acs.org/10.1021/acsnano.5c19751

Author Contributions

$^{\nabla}$X.L., L.X, and H.Y. contributed equally to this work, specifically participating in the design, synthesis, characterization of molecular materials as well as the mechanism research; additionally, Y.Z. and G.H. provided support for theoretical calculations, while J.W., Han.Y., He.Y., R.T.K.K., and J.S. were responsible for the verification of optical properties. The manuscript was written through contributions of all authors. All authors have given approval to the final version of the manuscript.

Notes

The authors declare no competing financial interest.

ACKNOWLEDGMENTS

We are grateful for the financial support from the National Natural Science Foundation of China (52303189, U22A20144, and 52333007), Key Research and Development Program of Yinchuan, Ningxia (2024SFZD004), and the Innovation and Technology Commission of Hong Kong (ITC−CNERC14SC01 and ITCPD/17-9), Natural Science Foundation of Ningxia Province (2023AAC05027), the National Key Research and Development Program of China (2023YFB3810001), Key-Area Research and Development Program of Guangdong Province (2024B0101040001), Shenzhen Key Laboratory of Functional Aggregate Materials (ZDSYS20211021111400001), and the Science Technology Innovation Commission of Shenzhen Municipality (KQTD20210811090142053). All animal experiments were approved by the laboratory animal research center of Ningxia University (Animal Welfare Assurance no. NXU2025057, Ningxia, China).

REFERENCES

(1) Tang, Y.; Li, Y.; Li, B.; Song, W.; Qi, G.; Tian, J.; Huang, W.; Fan, Q.; Liu, B. Oxygen-independent organic photosensitizer with ultralow-power NIR photoexcitation for tumor-specific photodynamic therapy. *Nat. Commun.* **2024**, *15* (1), No. 2530.

(2) Lei, S.; Huang, P. A photo-controlled charge regulator improves cancer theranostics. *Nat. Nanotechnol.* **2024**, *19* (11), 1585−1586.

(3) Zuo, L.; Nie, W.; Yu, S.; Zhuang, W.; Wu, G.; Liu, H.; Huang, L.; Shi, D.; Sui, X.; Li, Y.; Xie, H. Smart Tumor-Cell-Derived Microparticles Provide On-Demand Photosensitizer Synthesis and Hypoxia Relief for Photodynamic Therapy. *Angew. Chem., Int. Ed.* **2021**, *60* (48), 25365−25371.

(4) Ma, H.; Li, R.; Meng, H.; Tian, M.; Zhang, X.; Liu, Y.; Li, L.; Yuan, J.; Wei, Y. A Versatile Theranostic Nanoplatform with Aggregation-Induced Emission Properties: Fluorescence Monitoring, Cellular Organelle Targeting, and Image-Guided Photodynamic Therapy. *Small* **2023**, *19* (21), No. 2204778.

(5) Xiang, H.; Zhao, L.; Yu, L.; Chen, H.; Wei, C.; Chen, Y.; Zhao, Y. Self-Assembled Organic Nanomedicine Enables Ultrastable Photo-To-Heat Converting Theranostics in the Second Near-Infrared Biowindow. *Nat. Commun.* **2021**, *12* (1), No. 218.

(6) Li, B.; Wang, W.; Zhao, L.; Wu, Y.; Li, X.; Yan, D.; Gao, Q.; Yan, Y.; Zhang, J.; Feng, Y.; et al. Photothermal Therapy of Tuberculosis Using Targeting Pre-Activated Macrophage Membrane-Coated Nanoparticles. *Nat. Nanotechnol.* **2024**, *19* (6), 834−845.

(7) Ma, H.; Zhao, C.; Meng, H.; Li, R.; Mao, L.; Hu, D.; Tian, M.; Yuan, J.; Wei, Y. Multifunctional Organic Fluorescent Probe with Aggregation-Induced Emission Characteristics: Ultrafast Tumor Monitoring, Two-Photon Imaging, and Image-Guided Photodynamic Therapy. *ACS Appl. Mater. Interfaces* **2021**, *13* (7), 7987−7996.

(8) Cai, Y.; Chai, T.; Nguyen, W.; Liu, J.; Xiao, E.; Ran, X.; Ran, Y.; Du, D.; Chen, W.; Chen, X. Phototherapy in Cancer Treatment: Strategies and Challenges. *Signal Transduction Target. Ther.* **2025**, *10* (1), No. 115.

(9) Zhang, Z.; Du, Y.; Shi, X.; Wang, K.; Qu, Q.; Liang, Q.; Ma, X.; He, K.; Chi, C.; Tang, J.; et al. NIR-II Light in Clinical Oncology: Opportunities and Challenges. *Nat. Rev. Clin. Oncol.* **2024**, *21* (6), 449−467.

(10) Ding, Q.; Huang, S.; Zhang, Z.; Yu, D.; Li, M.; He, Q.; Mei, L. Integration of Photodiagnosis and Therapy Guided by Micro/Nanorobots. *Adv. Mater.* **2025**, *37* (18), No. 2420359.

(11) Ma, H.; An, Y.; Han, Y.; Zhao, F.; Zuo, Y.; He, G.; Lu, Z.; Kwok, R. T. K.; Sun, J.; Lam, J. W. Y. A "3 + 2" Cooperation Pattern of Amphipathic AIE Phototheranostic System for Multimodal Image-Guided Synergistic Type I/II Photodynamic-Photothermal Therapy. *Adv. Sci.* **2025**, No. e07956.

(12) Liang, S.; Liu, Y.; Zhu, H.; Liao, G.; Zhu, W.; Zhang, L. Emerging nitric oxide gas-assisted cancer photothermal treatment. *Exploration* **2024**, *4* (6), No. 20230163.

(13) Zhang, Z.; Li, X.; Yang, H.; You, C.; Ren, K.; Yang, Z.; Kang, M.; Wang, D.; Tang, B. Z. J. A. NIR-II AIEgens for High-Contrast

Intravital Fluorescence Angiography: Recent Advances and Prospects. *Aggregate* **2025**, *6* (8), No. e70102.

(14) Wang, M.; Bai, S.; Zhang, Y. Single-and multi-modal molecular probes with second near-infrared activatable optical signals for disease diagnosis and theranostics. *Chem. Soc. Rev.* **2025**, *54*, 7561−7609.

(15) He, L.; Li, Y.; Zhang, C.; Zhang, X.; Wang, B.; Ren, T.; Yuan, L. Development of small-molecule NIR-II photothermal agents for image-guided tumor therapy. *Coord. Chem. Rev.* **2025**, *533*, No. 216549.

(16) Shi, Y.; Chang, Y.; Lu, K.; Chen, Z.; Zhang, J.; Yan, Y.; Qiu, D.; Liu, Y.; Adil, M. A.; Ma, W.; et al. Small Reorganization Energy Acceptors Enable Low Energy Losses in Non-Fullerene Organic Solar Cells. *Nat. Commun.* **2022**, *13* (1), No. 3256.

(17) Shen, H.; Sun, F.; Zhu, X.; Zhang, J.; Ou, X.; Zhang, J.; Xu, C.; Sung, H. H. Y.; Williams, I. D.; Chen, S.; et al. Rational Design of NIR-II AIEgens with Ultrahigh Quantum Yields for Photo- and Chemiluminescence Imaging. *J. Am. Chem. Soc.* **2022**, *144* (33), 15391−15402.

(18) Niu, G.; Song, G.; Kang, Y.; Zhai, Y.; Fan, Y.; Ye, J.; Li, R.; Li, R.; Zhang, Y.; Wang, H.; et al. Quinoidal Semiconductor Nanoparticles for NIR-II Photoacoustic Imaging and Photoimmunotherapy of Cancer. *Adv. Mater.* **2025**, *37* (6), No. 2415189.

(19) Wang, Y.; Zhang, J.; Wang, Y.; Yu, J.; Gao, Y.; Yang, Y.; Li, X.; Wang, H.; Li, S. A NIR-II-Emissive Organic Nanomedicine with Biomimetic Engineering for High-Contrast Targeted Bioimaging and Multiple Phototherapies of Pancreatic Tumors. *Adv. Funct. Mater.* **2024**, *34* (41), No. 2406483.

(20) Li, C.; Jiang, G.; Yu, J.; Ji, W.; Liu, L.; Zhang, P.; Du, J.; Zhan, C.; Wang, J.; Tang, B. Z. Fluorination Enhances NIR-II Emission and Photothermal Conversion Efficiency of Phototheranostic Agents for Imaging-Guided Cancer Therapy. *Adv. Mater.* **2023**, *35* (3), No. 2208229.

(21) Yang, S.; Jia, Q.; Ou, X.; Sun, F.; Song, C.; Zhao, T.; Kwok, R. T. K.; Sun, J.; Zhao, Z.; Lam, J. W. Y.; et al. Integration of Motion and Stillness: A Paradigm Shift in Constructing Nearly Planar NIR-II AIEgen with Ultrahigh Molar Absorptivity and Photothermal Effect for Multimodal Phototheranostics. *J. Am. Chem. Soc.* **2025**, *147* (4), 3570−3583.

(22) Li, J.; Kang, M.; Zhang, Z.; Li, X.; Xu, W.; Wang, D.; Gao, X.; Tang, B. Z. Synchronously Manipulating Absorption and Extinction Coefficient of Semiconducting Polymers via Precise Dual-Acceptor Engineering for NIR-II Excited Photothermal Theranostics. *Angew. Chem., Int. Ed.* **2023**, *62* (20), No. e202301617.

(23) Zou, Y.; Liu, H.; Cai, L.; Li, Y.; Hu, J.; Liu, C.; Liu, T. Strategy to Efficient Photodynamic Therapy for Antibacterium: Donor-Acceptor Structure in Hydrogen-Bonded Organic Framework. *Adv. Mater.* **2024**, *36* (35), No. 2406026.

(24) Wu, Y.; Yu, H.; Li, C.; Liu, L.; Zhang, Y.; Gong, J.; Sha, R.; Feng, L.; Yan, H.; Jiang, G.; et al. Spacer Twisting Strategy to Realize Ultrabright Near-Infrared II Polymer Nanoparticles for Fluorescence Imaging-Guided Tumor Phototheranostics. *ACS Nano* **2024**, *18* (41), 28178−28188.

(25) Lu, H.; Li, D.; Liu, W.; Ran, G.; Wu, H.; Wei, N.; Tang, Z.; Liu, Y.; Zhang, W.; Bo, Z. Designing A−D−A Type Fused-Ring Electron Acceptors with a Bulky 3D Substituent at the Central Donor Core to Minimize Non-Radiative Losses and Enhance Organic Solar Cell Efficiency. *Angew. Chem., Int. Ed.* **2024**, *63* (33), No. e202407007.

(26) Ma, Y.; Zheng, Q. ADA-Type Electron Acceptors Based on Pyrrole-Containing Ladder-Type Heteroarenes for Organic Solar Cells. *Innov. Mater.* **2023**, *1* (3), No. 100044.

(27) Shao, W.; Zhao, F.; Xue, J.; Huang, L. NIR-II Absorbing Organic Nanoagents for Photoacoustic Imaging and Photothermal Therapy. *BMEMat* **2023**, *1* (1), No. e12009.

(28) Guo, S.; Gu, D.; Yang, Y.; Tian, J.; Chen, X. Near-Infrared Photodynamic and Photothermal Co-Therapy Based on Organic Small Molecular Dyes. *J. Nanobiotechnol.* **2023**, *21* (1), No. 348.

(29) Chu, Y.; Liao, S.; Liao, H.; Lu, Y.; Geng, X.; Wu, D.; Pei, J.; Wang, Y. Second Near-Infrared Photothermal Therapy with Superior Penetrability through Skin Tissues. *CCS Chem.* **2022**, *4* (9), 3002−3013.

(30) Xie, X.; Wang, K.; Zeng, J.; Xu, M. Y.; Qu, X. H.; Xiang, Z. B.; Tou, F. F.; Huang, S. R.; Han, X. J. A Novel Polymer Enabled by Polymerized Small Molecule Strategy for Tumor Photothermal and Photodynamic Therapy. *J. Nanobiotechnol.* **2023**, *21* (1), No. 497.

(31) Xu, R.; Shen, Q.; Zhang, P.; Wang, Z.; Xu, Y.; Meng, L.; Dang, D. Less is More: Asymmetric D−A Type Agent to Achieve Dynamic Self-Assembled Nanoaggregates for Long-Acting Photodynamic Therapy. *Adv. Mater.* **2024**, *36* (28), No. 2402434.

(32) Giannini, S.; Sowood, D. J. C.; Cerdá, J.; Frederix, S.; Grüne, J.; Londi, G.; Marsh, T.; Ghosh, P.; Duchemin, I.; Greenham, N. C.; et al. On the Role of Charge Transfer Excitations in Non-Fullerene Acceptors for Organic Photovoltaics. *Mater. Today* **2024**, *80*, 308−326.

(33) Gu, Y.; Lai, H.; Chen, Z.; Zhu, Y.; Sun, Z.; Lai, X.; Wang, H.; Wei, Z.; Chen, L.; Huang, L.; et al. Chlorination-Mediated $\pi-\pi$ Stacking Enhances the Photodynamic Properties of a NIR-II Emitting Photosensitizer with Extended Conjugation. *Angew. Chem., Int. Ed.* **2023**, *135* (25), No. e202303476.

(34) Ma, F.; Jia, Q.; Deng, Z.; Wang, B.; Zhang, S.; Jiang, J.; Xing, G.; Wang, Z.; Qiu, Z.; Zhao, Z.; Tang, B. Z. Boosting Luminescence Efficiency of Near-Infrared-II Aggregation-Induced Emission Luminogens via a Mash-Up Strategy of π-Extension and Deuteration for Dual-Model Image-Guided Surgery. *ACS Nano* **2024**, *18* (13), 9431−9442.

(35) Mahadevan, S.; Liu, T.; Pratik, S. M.; Li, Y.; Ho, H. Y.; Ouyang, S.; Lu, X.; Yip, H.-L.; Chow, P. C. Y.; Brédas, J.-L.; et al. Assessing intra- and inter-molecular charge transfer excitations in non-fullerene acceptors using electroabsorption spectroscopy. *Nat. Commun.* **2024**, *15* (1), No. 2393.

(36) Lee, K. W.; Gao, Y. J.; Chou, S. H.; Wan, Y. P.; Hsu, A. C. H.; Tan, J. H.; Li, Y. Q.; Guan, Z. Q.; Chen, H.; Li, S. L.; et al. Construction of Through-Space Charge-Transfer Nanoparticles for Facilely Realizing High-Performance NIR-II Cancer Phototheranostics. *Adv. Funct. Mater.* **2024**, *34* (45), No. 2407317.

(37) Yang, H.; Sun, Z.; Zhang, Z.; Song, S.; Wen, H.; Yang, Z.; Li, X.; Xiang, S.; Wang, L.; Kang, M.; et al. NIR-II Multimodal Phototheranostics Synergized with Antigen-Specific Vaccines for Boosted Cancer Photoimmunotherapy. *ACS Nano* **2026**, *20*, 1928−1944, DOI: 10.1021/acsnano.5c12430.

(38) Zhuang, J.; Ma, Z.; Li, N.; Chen, H.; Yang, L.; Lu, Y.; Guo, K.; Zhao, N.; Tang, B. Z. Molecular Engineering of Plasma Membrane and Mitochondria Dual-Targeted NIR-II AIE Photosensitizer Evoking Synergetic Pyroptosis and Apoptosis. *Adv. Mater.* **2024**, *36* (5), No. 2309488.

(39) Zhao, C. H.; Liu, Z. K.; Chang, C. C.; Chen, Y.-C.; Zhang, Q.; Zhang, X. D.; Andreou, C.; Pang, J. D.; Liu, Z. X.; Wang, D. Y.; et al. Near-Infrared Phototheranostic Iron Pyrite Nanocrystals Simultaneously Induce Dual Cell Death Pathways via Enhanced Fenton Reactions in Triple-Negative Breast Cancer. *ACS Nano* **2023**, *17* (5), 4261−4278.

(40) Wang, B.; Zhou, H.; Chen, L.; Ding, Y.; Zhang, X.; Chen, H.; Liu, H.; Li, P.; Chen, Y.; Yin, C. A Mitochondria-Targeted Photosensitizer for Combined Pyroptosis and Apoptosis with NIR-II Imaging/Photoacoustic Imaging-Guided Phototherapy. *Angew. Chem., Int. Ed.* **2024**, *63* (39), No. e202408874.

(41) Yao, S.; Xu, F.; Wang, Y.; Shang, J.; Li, S.; Xu, X.; Liu, Z.; He, W.; Guo, Z.; Chen, Y. Photoinduced Synergism of Ferroptosis/Pyroptosis/Oncosis by an O_2-Independent Photocatalyst for Enhanced Tumor Immunotherapy. *J. Am. Chem. Soc.* **2025**, *147* (13), 11132−11144.

(42) Xu, X.; Shabiti, S.; Zhang, X.; Zheng, J.; Liang, N.; Wang, Z.; Yu, S.; Wang, Y.; Jiang, S.; Pan, Z.; et al. Membrane-Anchoring Clickable Iridium(III) Nanosonosensitizer In Situ Evokes PANoptosis for Augmented Tumor Sono-Immunotherapy. *Nano Today* **2024**, *56*, No. 102270.

(43) Wang, H.; Qiao, C.; Guan, Q.; Wei, M.; Li, Z. Nanoparticle-Mediated Synergistic Anticancer Effect of Ferroptosis and Photo-

dynamic Therapy: Novel Insights and Perspectives. *Asian J. Pharm. Sci.* **2023**, *18* (4), No. 100829.

(44) Chen, J.; Duan, Z.; Deng, L.; Li, L.; Li, Q.; Qu, J.; Li, X.; Liu, R. Cell Membrane-Targeting Type I/II Photodynamic Therapy Combination with FSP1 Inhibition for Ferroptosis-Enhanced Photodynamic Immunotherapy. *Adv. Healthcare Mater.* **2024**, *13* (16), No. 2304436.

(45) Lorenz, S. M.; Wahida, A.; Bostock, M. J.; Seibt, T.; Santos Dias Mourão, A.; Levkina, A.; Trümbach, D.; Soudy, M.; Emler, D.; Rothammer, N.; et al. A fin-loop-like structure in GPX4 underlies neuroprotection from ferroptosis. *Cell* **2025**, *S0092−8674* (25), 01310−01318.

(46) Gao, L.; Shay, C.; Teng, Y. Cell Death Shapes Cancer Immunity: Spotlighting PANoptosis. *J. Exp. Clin. Cancer Res.* **2024**, *43* (1), No. 168.

(47) Diao, J.; Jia, Y.; Dai, E.; Liu, J.; Kang, R.; Tang, D.; Han, L.; Zhong, Y.; Meng, L. Ferroptotic Therapy in Cancer: Benefits, Side Effects, and Risks. *Mol. Cancer* **2024**, *23* (1), No. 89.

(48) Zhou, L.; Lyu, J.; Liu, F.; Su, Y.; Feng, L.; Zhang, X. Immunogenic PANoptosis-Initiated Cancer Sono-Immune Reediting Nanotherapy by Iteratively Boosting Cancer Immunity Cycle. *Adv. Mater.* **2024**, *36* (2), No. 2305361.

(49) Fu, Y.; Lee, T. H.; Chin, Y. C.; Pacalaj, R. A.; Labanti, C.; Park, S. Y.; Dong, Y.; Cho, H. W.; Kim, J. Y.; Minami, D.; et al. Molecular Orientation-Dependent Energetic Shifts in Solution-Processed Non-Fullerene Acceptors and Their Impact on Organic Photovoltaic Performance. *Nat. Commun.* **2023**, *14* (1), No. 1870.

(50) Zhang, Q.; Zheng, Y. J.; Sun, W.; Ou, Z.; Odunmbaku, O.; Li, M.; Chen, S.; Zhou, Y.; Li, J.; Qin, B.; Sun, K. High-Efficiency Non-Fullerene Acceptors Developed by Machine Learning and Quantum Chemistry. *Adv. Sci.* **2022**, *9* (6), No. 2104742.

(51) Kim, M.; Ryu, S. U.; Park, S. A.; Pu, Y. J.; Park, T. Designs and Understanding of Small Molecule-Based Non-Fullerene Acceptors for Realizing Commercially Viable Organic Photovoltaics. *Chem. Sci.* **2021**, *12* (42), 14004−14023.

(52) Du, T.; Zhang, X.; Du, M.; Guo, Q.; Guo, Q.; Zhou, E. Fused Benzotriazole as the A′ Unit to Construct A−D−A′−D−A-Type Non-Fused Ring Electron Acceptors for Efficient Organic Solar Cells. *J. Mater. Chem. A* **2025**, *13* (25), 19297−19306.

(53) Schmitt, H. L.; Martymianov, D.; Green, O.; Delcaillau, T.; Park Kim, Y. S.; Morandi, B. Regiodivergent Ring-Expansion of Oxindoles to Quinolinones. *J. Am. Chem. Soc.* **2024**, *146* (7), 4301−4308.

(54) Bhunia, S.; Peña-Duarte, A.; Li, H.; Li, H.; Sanad, M. F.; Saha, P.; Addicoat, M. A.; Sasaki, K.; Strom, T. A.; Yacamán, M. J.; et al. [2,1,3]-Benzothiadiazole-Spaced Co-Porphyrin-Based Covalent Organic Frameworks for O_2 Reduction. *ACS Nano* **2023**, *17* (4), 3492−3505.

(55) Liang, M.; Liu, L.; Sun, Y.; Li, J.; Zhang, Le.; Jiang, X.; Wu, W. Furan-modified thiadiazolo quinoxaline as an electron acceptor for constructing second near-infrared aggregation-induced emission fluorophores for beyond 1300 nm fluorescence/photoacoustic imaging and photothermal therapy. *Aggregate* **2024**, *5* (2), No. e458.

(56) Feng, L.; Tuo, Y.; Wu, Z.; Zhang, W.; Li, C.; Yang, B.; Liu, L.; Gong, J.; Jiang, G.; Hu, W.; et al. Highly Stable Near-Infrared II Luminescent Diradicaloids for Cancer Phototheranostics. *J. Am. Chem. Soc.* **2024**, *146* (47), 32582−32594.

(57) Yan, J.; Rodríguez-Martínez, X.; Pearce, D.; Douglas, H.; Bili, D.; Azzouzi, M.; Eisner, F.; Virbule, A.; Rezasoltani, E.; Belova, V.; et al. Identifying structure−absorption relationships and predicting absorption strength of non-fullerene acceptors for organic photovoltaics. *Energy Environ. Sci.* **2022**, *15* (7), 2958−2973.

(58) Wang, Y.; Chai, C.; Lin, W.; Cao, J.; Li, Z.; Jin, Y.; Xu, Y.; Zhang, J.; Qu, Y.; Zhan, J.; et al. Oxidative stress-mediated PANoptosis and ferroptosis: Exploration of multimodal cell death triggered by an AIE-active nano-photosensitizer via photodynamic therapy. *Theranostics* **2025**, *15* (14), 6665−6685.

(59) Ma, C.; Gao, L.; Song, K.; Gu, B.; Wang, B.; Yu, Y.; Wang, X.; Li, X.; Hu, J.; Pu, W.; et al. Targeted Dual-Responsive Liposomes Co-Deliver Jolkinolide B and Ce6 to Synergistically Enhance the Photodynamic/Immunotherapy Efficacy in Gastric Cancer through the PANoptosis Pathway. *Adv. Sci.* **2025**, *12* (29), No. e02289.

(60) Dos Santos, A. F.; Inague, A.; Arini, G. S.; Terra, L. F.; Wailemann, R. A. M.; Pimentel, A. C.; Yoshinaga, M. Y.; Silva, R. R.; Severino, D.; de Almeida, D. R. Q.; et al. Distinct photo-oxidation-induced cell death pathways lead to selective killing of human breast cancer cells. *Cell Death Dis.* **2020**, *11* (12), No. 1070.